12-2019

SOLID STATE SYNTHESIS OF MULTICOMPONENT RARE-EARTH OXIDE CERAMICS

Matheus Pianassola
University of Tennessee, mpianass@vols.utk.edu

To the Graduate Council:

I am submitting herewith a thesis written by Matheus Pianassola entitled "SOLID STATE SYNTHESIS OF MULTICOMPONENT RARE-EARTH OXIDE CERAMICS." I have examined the final electronic copy of this thesis for form and content and recommend that it be accepted in partial fulfillment of the requirements for the degree of Master of Science, with a major in Materials Science and Engineering.

Mariya Zhuravleva, Major Professor

We have read this thesis and recommend its acceptance:

Charles Melcher, Veerle Keppens

Accepted for the Council:
Dixie L. Thompson

Vice Provost and Dean of the Graduate School

(Original signatures are on file with official student records.)

SOLID-STATE SYNTHESIS OF MULTICOMPONENT RARE-EARTH OXIDE CERAMICS

A Thesis Presented for the
Master of Science
Degree
The University of Tennessee, Knoxville

Matheus Pianassola
December 2019

ACKNOWLEDGEMENTS

I would like to express my sincere gratitude to Dr. Charles Melcher and Dr. Mariya Zhuravleva for mentoring me through my graduate school journey with their motivation, inspiration, and support. A special thanks to Mrs. Merry Koschan for patiently investing time helping me develop my communication skills and also for her important contribution to my research. Thank you to Dr. Veerle Keppens for being part of my thesis committee and for sharing her time and valuable suggestions.

I would like to thank our collaborator Dr. Jake McMurray from Oak Ridge National Lab for his insightful comments and for being interested in this project. I am also thankful for my colleagues in the Scintillation Materials Research Center: Dr. Luis Stand, Dr. Yuntao Wu, Dr. Fang Meng, Dr. Matthew Loyd, Camera Foster, Kaycee Gass, Daniel Rutstrom, Josh Smith, Eleanor Comer, and Cordell Delzer. Thank you for helping me find my way around the labs and for the advice and discussions. I was also fortunate to have Madeline Loveday working closely on this project; this work would not have been possible without her help and patience.

Thank you to the UT staff that made this work possible: Carla Lawrence, Ashley Cole, Tonya Goins, Frank Holiway, Randy Stooksbury, Doug Fielden, Larry Smith, and Adam Cain.

I would like to acknowledge our funding sources for their support. This work is supported by the National Science Foundation under the award DMR-1846935. I also acknowledge the financial support of Siemens Medical Solutions for their contributions to the Scintillation Materials Research Center.

Many of the results in this thesis have been submitted in a peer-reviewed journal by Matheus Pianassola. A citation of the submitted manuscript is as follows: M. Pianassola, M. Loveday, J.W. McMurray, M. Koschan, C.L. Melcher, M.

Zhuravleva. Solid-state synthesis of multicomponent equiatomic rare-earth oxides. Submitted to Journal of The American Ceramic Society in October 2019. The author would like to acknowledge the efforts and contributions of the co-authors.

XRD measurements were performed at the JIAM Diffraction Facility with the collaboration of Dr. Michael Koehler. EPMA measurements were performed at the Electron Microprobe Laboratory in the Earth and Planetary Sciences Dept. with the collaboration of Dr. Molly McCanta and Dr. Allan Patchen. XPS measurements were performed at the JIAM Advanced Photoelectron Spectrometer Facility with the collaboration of Dr. Norman Manella and Dr. Paolo Vilmercati. EDS measurements were performed at the Jiam Electron Microscopy Facility with the collaboration of Dr. John Dunlap.

ABSTRACT

Multicomponent rare-earth oxide ceramics with various equiatomic combinations of Ce, Gd, La, Nd, Pr, Sm, and Y were produced by solid-state synthesis. The effects of composition, sintering atmosphere, and cooling rate on the crystal structure are studied. With a slow cooling of 3.3 ºC/min, single cubic or monoclinic phase compositions can be obtained, showing that rare-earth oxides have a different phase stabilization mechanism when compared to transition metal high-entropy oxides. A cubic phase is induced by both Ce and Pr when the ceramic is synthesized in an oxidizing atmosphere; only Ce has this effect in an inert or reducing atmosphere. Samples that do not contain Ce or Pr form a single monoclinic phase. When the ceramics are annealed in an atmosphere different than the original sintering atmosphere, the phases formed at initial synthesis may be converted to a different one. Additionally, the phase transition of a five-cation composition was investigated as a function of sintering temperature in air. At 1450ºC all the five binary oxides used as raw materials dissolve into a single cubic structure.

TABLE OF CONTENTS

LIST OF TABLES

LIST OF FIGURES

CHAPTER ONE
INTRODUCTION

High-entropy materials

High-entropy metallic alloys

Traditional metallic alloys are composed of a mixture of a principal element and relatively small amounts of alloying elements. Usually, the alloying elements improve the physical, chemical, and mechanical properties of the pure principal metal, which makes the alloys more appropriate for specific applications. The chemical composition of traditional alloys lies on the extremities of the phase diagrams, which means that the concentration of alloying elements is relatively low [1], [2]. Figure 1.1 shows a schematic representation of ternary and quaternary phase diagrams, where the green corners indicate compositional regions that are explored in traditional alloys [2]. All figures and tables are located in the appendix.

The central region of the diagrams in Figure 1.1 remained unexplored until 2004, when Cantor [3] and Yeh [4] independently reported on an innovative approach of alloy engineering that consisted in mixing at least five metallic elements in equiatomic amounts. Based on the behavior of conventional alloys, one would expect a complex structure and several intermetallic compounds in the equiatomic alloys. However, Cantor [3] and Yeh [4] obtained single-phase solid solutions. Yeh [4] named this new alloy concept “high-entropy alloys” (HEA) due to the high configurational entropy of these materials at their random solution state.

The specific compositions and crystal structures reported by Cantor and Yeh are as follows. Cantor [3] produced an equiatomic FeCrMnNiCo alloy with a single FCC structure. By adding other elements such as Nb, Ti, V, Cu, and Ge, the alloys containing six to nine components formed a multiphase structure with a primary FCC phase. Yeh [4] reported on an $CuCoNiCrAl_xFe$ alloy that developed a simple

FCC structure for aluminum concentrations from x = 0 to x = 0.5, a mixture of FCC and BCC structures from x = 0.8 to x = 2.5, and a single BCC structure for x > 2.8. The values of hardness for compositions containing from 6 to 9 elements were substantially superior to those of conventional alloys such as 17-4 PH stainless steel and Ti-6Al-4V.

Those two first publications introduced an alternative to the conventional alloy design strategies and instigated a considerable amount of investigation of metallic compositional spaces that were previously unexplored. Since 2014, hundreds of papers have been published on HEA [2]. The formal definition of HEA has been developed by Yeh [4] and Otto [5]; the definition states that a HEA is a single-phase disordered solution composed of at least five principal elements with concentrations between 5 and 35 at.%.

In various compositional systems of HEA, remarkable properties were found and attributed to what Ranganathan [6] called the “cocktail effect”. The expression “cocktail effect” addresses the synergistic mixture that results in HEA with exceptional properties that are greater than those predicted by the rule of mixing. Such properties include hardness [7]–[9], tensile strength [10]–[12], electrical resistivity [13]–[15], superconductivity [16], [17], and magnetism [18], [19].

Thermodynamic principles of phase stability

Observing the principles of physical metallurgy, one would expect an HEA to form binary, ternary, quaternary compounds; the interactions among the constituent elements would also form segregated phases. However, this assumption is no longer valid if the effects of high entropy of mixing are considered [1], [2], [6]. In a metallic alloy, the equilibrium state consists in a phase or a combination of phases with the lowest Gibbs energy among all the many competing phases. The Gibbs free energy of mixing ΔG_{mix} is defined in Equation 1 where ΔH_{mix} is the enthalpy of mixing, T is the absolute temperature, and ΔS_{mix} is the entropy of mixing [2].

$$\Delta G_{mix} = \Delta H_{mix} - T\Delta S_{mix} \qquad \text{Equation 1}$$

In Equation 1, a competition between ΔH_{mix} and $T\Delta S_{mix}$ defines the equilibrium phase with the lowest ΔG_{mix}. The enthalpy of mixing ΔH_{mix} can be estimated as shown in Equation 2, where N is the number of elements, ΔH_{AB}^{mix} is the enthalpy of mixing for the binary equiatomic AB alloys, and x_i or x_j are the molar concentration of the i^{th} or j^{th} element, respectively [1].

$$\Delta H_{mix} = \sum_{i=1,\ i\neq j}^{N} 4\Delta H_{AB}^{mix} x_i x_j \qquad \text{Equation 2}$$

The entropy of mixing ΔS_{mix} includes the configurational, magnetic, electronic, and vibrational entropy contributions. In HEA, the configurational entropy ΔS_{conf} plays a key role in maximizing ΔS_{mix} [1]. An expression for ΔS_{conf} is defined in Equation 3, where R is the gas constant. This expression uses the Boltzmann equation, assuming that the HEA is in the liquid or fully random solid solution state.

$$\Delta S_{conf} = -R \sum_{i=1}^{N} x_i \ln x_i \qquad \text{Equation 3}$$

ΔS_{conf} can be maximized by having the n principal elements in equimolar ratios; this case is derived in Equation 4 by making $x_i = 1/n$ [2]. Figure 1.2 illustrates how ΔS_{conf} (Equation 3) is maximum at the equimolar composition for a binary system with components A and B. The values of configurational entropies have been classified by Yeh [20] in three categories: low entropy for $\Delta S_{conf} \leq 1R$, medium entropy for $1R < \Delta S_{conf} < 1.5R$, and high entropy for $\Delta S_{conf} \geq 1.5R$. Therefore, according to Equation 4, only alloys with 5 or more elements in equimolar amounts can be classified as high-entropy since $ln(5) \cong 1.6$.

$$\Delta S_{conf} = -R\left(\frac{1}{n}\ln\frac{1}{n} + \frac{1}{n}\ln\frac{1}{n} + \cdots + \frac{1}{n}\ln\frac{1}{n}\right) = R\ln n \qquad \text{Equation 4}$$

The Gibbs free energy of mixing ΔG_{mix} defined in Equation 1 can be significantly

minimized at elevated temperatures by the contribution of high configurational entropies ΔS_{conf}. Lower values of ΔG_{mix} decrease the tendency to segregate and promotes the ordering of the elements in a HEA during solidification, favoring the formation of solid solutions rather than intermetallic compounds [1].

High configurational entropies also promote a lower number of stable phases than the one predicted by the Gibbs phase rule. Equation 5 shows the Gibbs phase rule, which correlates the number of phases P, the degrees of freedom F, and the number of components C. The Gibbs phase rule states that the maximum number of phases possible in a system is $C + 1$, therefore a HEA with five components cannot have more than six phases. However, when those components are taken in equimolar amounts, a single phase may be observed, making the number of stable phases well below the maximum possible [1], [2].

$$P + F = C + 1 \qquad \text{Equation 5}$$

The high-entropy concept applied to other classes of materials

The unexpected and exceptional properties of HEA inspired recent efforts to extend the concept of high entropy stabilization toward other classes of materials. A schematic representation of the “materials world” proposed by Murty [2], seen in Figure 1.3, divides the research space into three major classes of materials: alloys, ceramics, and polymers. Each class of materials is subdivided into three regions based on the configurational entropy category: low, medium, and high entropy. Murty’s representation of the “materials world” encourages the applied research to migrate from the central low-entropy region towards the high-entropy borders. As in the case of alloys, attractive functional properties might be found in the largely unexplored high-entropy regions of ceramics and polymers.

The first attempts to apply the high-entropy effect outside of the alloy research area focused on nitrides. Lai [21] reported on a multielement nitride (Al,Cr,Ta,Ti,Zr)N

film with a single FCC structure. The film was deposited on cemented carbide plates by reactive RF magnetron sputtering. Attractive hardness and adhesion values were found, making this type of multicomponent nitride a promising candidate for a coating to enhance the lifetime of tools for machining.

A high-entropy carbide (Ti,Al,Cr,Nb,Y)C was also reported as a new type of protective coating by Braic [22]. The film was prepared by reactive co-sputtering and a single FCC phase was formed. In this primary research, the hardness values of the multicomponent carbide were lower than those of the binary carbides; however, the dry friction coefficients were promising.

High-entropy metal diborides have been recently reported by Gild [23] as a new type of ultrahigh temperature ceramic. Seven five-component diboride compositions containing different combinations of Hf, Mo, Nb, Ta, Ti, Zr were produced by spark plasma sintering. All samples had a single hexagonal phase. The hardness and oxidation resistance of the high-entropy compositions were higher than the average performance of the binary diborides.

Rost [24] recently launched the field of high-entropy oxides by reporting a single rock salt structure for (Mg,Ni,Co,Cu,Zn)O pellets produced by solid-state synthesis. Only samples quenched from temperatures above 900ºC developed a single phase, confirming the entropy-driven stabilization of the single phase; in addition, a multiphase structure was induced by annealing single phase samples at 750ºC.

Since Rost's report on (Mg,Ni,Co,Cu,Zn)O [24], the field of high-entropy oxides has attracted special attention due to the functional properties found in oxides such as luminescent, piezoelectric, dielectric, ferroelectric, and ferromagnetic behaviors [25]. Some functional properties reported for high-entropy oxide systems include high dielectric constant [26], lithium superionic conductivity [27], magnetic properties [28]–[30], electrical and thermal conductivities [31], [32], reversible energy storage [33], and high catalytic activity in CO oxidation [34].

Multicomponent rare-earth oxides

Rare-earth oxides

In the field of high-entropy oxides, the specific compositional space of rare-earth oxides attracts attention. Many functional properties are attributed to rare-earth oxides, making them suitable for luminescence activation, high-temperature superconductors, electroceramics, ferroelectric materials, and permanent magnets [35]. Given that, an intense exploration of multicomponent rare-earth oxides by engineering the atomic mixing on the cation sublattice may reveal promising functional properties for this compositional space.

Rare-earth binary oxides have six distinct crystalline structures. In ambient conditions, four structures can be found. Three of the rare earth elements (Ce, Pr, Tb) form a fluorite structure (space group Fm-3m) in their most oxidized state REO_2, where RE represents a rare-earth element. All rare-earth elements form polymorphic sesquioxides (RE_2O_3); a phase diagram is shown in Figure 1.4. Below 2000ºC, three crystal structures are observed: a hexagonal A-type structure for lighter sesquioxides (La - Pm), a monoclinic B-type structure for medium size cations (Sm - Gd), and a cubic C-type structure for small cation radii (Tb - Lu and Y). The space groups of the structures A, B, and C are P-3m1, C2, and Ia-3, respectively. Table 1.1 shows the binary oxides used in this work correlated with their cation oxidation state, the four possible crystal structures, coordination number, and cationic radii.

The high-entropy concept applied to rare-earth oxides

Djenadic [36] was the pioneer in the exploration of multicomponent rare-earth oxides. Nanocrystalline powder samples containing different combinations of Ce, Gd, La, Nd, Pr, Sm, and Y oxides taken in equiatomic ratios were synthesized by

nebulized spray pyrolysis. The experimental setup used is shown in Figure 1.5. Water-based solutions of rare-earth nitride salts were used as precursors and added in the nebulizer. The mist containing droplets of the precursors was transported by flowing oxygen through a hot-wall reactor at 1150ºC. The nanoparticles were collected in the filter particle collector.

In Djenadic's [36] work, compositions containing Ce and with less than 7 type rare-earth cations developed a single fluorite structure. Samples without Ce and with any number of cations did not crystallize in a single phase, indicating that this element has a vital importance in phase stabilization. Since CeO_2 has the fluorite structure found in the multicomponent samples, CeO_2 had the parent structure into which the other rare-earth oxides dissolve by substitution in the cation sublattice. Djenadic [36] also selected some compositions with 6 or 7 types of cations to perform annealing experiments in air at 1000°C for 1 h with cooling rates of 10 °C/min. Those samples had a phase transition from single fluorite structure to single bixbyite structure (which is a fluorite-related structure). This phase transition is attributed to the formation of oxygen vacancies during the annealing experiments.

In summary, Djenadic [36] found that the rare-earth oxide systems have two surprising characteristics: the importance of one element (Ce) in the phase stabilization and the possibility of maintaining a single structure after slow cooling from the annealing experiments. These two characteristics make this class of high-entropy oxides unique. The transition-metal high-entropy oxides that had been previously reported generally have a reversible phase transition when annealed, from single to multiphase. In addition, no vital element for phase stabilization had been reported for high-entropy oxides [24], [26], [32], [37]–[39]. Therefore, the phase formation mechanism is unique in multicomponent rare-earth oxides. For this reason, Djenadic reported the system as "multicomponent equiatomic rare-earth oxides" instead of "high-entropy rare-earth oxides".

Djenadic's group [40] further investigated the multicomponent rare-earth oxide

system and reported a narrow band gap and associated praseodymium multivalence in their samples, which may guide future exploration of the potential applications.

Tseng [41] recently published a high-entropy rare-earth sesquioxide $Gd_{0.4}Tb_{0.4}Dy_{0.4}Ho_{0.4}Er_{0.4}O_3$ produced by a polymeric steric entrapment method, which uses a solution of rare-earth nitride salts as a precursor. Even though the composition did not contain Ce, a single bixbyite structure was found, and no phase transformation was observed when the sample was annealed and cooled slowly. The phase stability was attributed to the small cationic radii difference between the five rare-earth elements, which was within 5%. Besides that, all the five rare-earths of that composition form individual binary sesquioxides with a bixbyite structure.

Multicomponent rare-earth oxides have not yet been explored by solid-state synthesis. Starting with binary oxides that have similar crystal structures may facilitate the formation of a single crystal structure. Additionally, the phase transitions that occur with increasing temperature (Figure 1.4) may induce the diffusion of the cations into a single crystal lattice.

The solid-state reaction also allows the cations to be oxidized or reduced during synthesis, favoring a preferential structure that may be different from the structure of the initial binary oxide. The multivalence of some of the rare-earth elements, such as Ce (3+ and 4+) and Pr (3+ and 4+) could affect the dissolution of different binary oxides into a single lattice.

CHAPTER TWO
OBJECTIVE AND MOTIVATION

Objective

The objective of this work is to study the phase formation in multicomponent equiatomic rare-earth oxide ceramics containing Ce, Gd, La, Nd, Pr, Sm, and Y produced by solid-state synthesis. The effects of the following parameters will be investigated: composition (number and type of rare-earth elements), sintering atmosphere (oxidizing, inert, and reducing), and cooling rate (slow cooling and air quenching). The phase convertibility and reversibility will be tested by annealing synthesized samples in different atmospheres.

Motivation

The study the phase formation in multicomponent rare-earth oxides is a first step in the exploration of the potential benefit of the cocktail effect in improving functional properties. This compositional space was chosen with the final purpose of investigating possible applications as optical or scintillation materials. Some of the most efficient luminescent activators are rare-earth elements, such as Ce^{3+} and Pr^{3+}. These activators can easily substitute for other rare-earth elements in optical materials. By exploring the high-entropy effect and by electronic band gap engineering, doped high-entropy oxides might reveal interesting optical and scintillation properties. Rare-earth oxides also have a relatively high density, which is a desired characteristic for x-ray and gamma-ray detection. The results of this study will be used to inform future parameters for crystal growth via the micro pulling down method.

CHAPTER THREE
EXPERIMENTAL METHODS

All synthesis experiments were performed at the Scintillation Materials Research Center. Table 3.1 shows the binary oxide powders used as raw materials, their manufacturer, purity, and initial crystal structure. All of the four ambient-condition structures of RE oxides can be found among the seven binary oxide powders used, namely the fluorite, A-, B-, and C-type structures. The raw powders were mixed to produce multicomponent samples with the general stoichiometry of a sesquioxide RE_2O_3. The rare-earth elements were taken in equiatomic amounts to compose the RE site. The mixtures were manually ground in an agate mortar, pressed into 13 mm-diameter 1 g pellets and then sintered in a furnace with atmosphere control. The sintering parameters varied according to the proposed experiments, as described in the “Solid-state synthesis” section.

Solid-state synthesis

Effects of composition on phase formation in samples sintered in air

In order to study the effects of elemental compositions and phases formed, various compositions were selected based the presence or absence of Ce and Pr and on the total number of cations. For this study, pellets were synthesized by sintering in air at 1500ºC for 10 h with a slow cooling rate of 3.3 ºC/min. Table 3.2 shows some examples of the compositions of this first set of samples. Here the samples are named according to the cations present and not to their stoichiometry, following Djenadic’s [36] labeling style. The rare-earth elements in each sample are taken in equiatomic amounts.

Experiments on the reaction sequence in (Ce,La,Pr,Sm,Y)O

The second set of samples discussed focused on the reaction sequence between the binary oxides in (Ce,La,Pr,Sm,Y)O and the phase evolution as a function of sintering temperature. This composition was selected because it has the maximum number of cations (five) that could be stabilized in a single crystal structure. Pellets of (Ce,La,Pr,Sm,Y)O were sintered in air for 10 h with a cooling rate of 3.3 ºC/min. The sintering temperatures used were within the range of 1000 - 1500 ºC.

Experiments on the effects of cooling rate on phase formation

To study the effects of cooling rate on phase formation, two compositions that form two different phases when cooled slowly were chosen: (Ce,Gd,La,Pr,Sm,Y)O and (Gd,La,Nd,Pr,Sm,Y)O. Pellets of those compositions were sintered in air at 1500ºC for 10 hours. The samples were cooled to room temperature in one of two ways: a slow cooling rate of 3.3 ºC/min or rapid cooling to 800ºC achieved by turning off the furnace followed by air quenching by extracting the samples from the furnace.

Experiments on the effects of sintering atmosphere on phase formation

Three sintering atmospheres were used to study their effects on phase formation: air (oxidizing), nitrogen (inert), or 2% hydrogen in bulk nitrogen (reducing). For this study pellets were sintered in one of those three atmospheres at 1500ºC for 10 h, with a cooling rate of 3.3 ºC/min. The representative compositions selected for this experiment have different types and number of cations and different crystal structures when sintered in air.

Experiments on the convertibility of phases with annealing atmosphere

Two atmospheres were used to assess the convertibility of phases with post-synthesis annealing atmosphere: air and 2% hydrogen in bulk nitrogen. For this experiment pellets were first synthesized by sintering in one of the atmospheres

followed by an annealing step in the other atmosphere. Both sintering and annealing steps were performed at 1500ºC for 10 h with a cooling rate of 3.3 ºC/min. Four representative compositions were selected due to their ability of forming distinct crystal structures depending on the sintering atmosphere: (Ce,La,Pr)O, (La,Pr)O, (Gd,La,Pr,Y)O, and (Ce,Gd,La,Nd,Pr,Sm, Y)O.

Characterization

Phase analysis with powder X-ray diffraction (XRD)

XRD measurements were performed at the JIAM Diffraction Facility with the collaboration of Dr. Koehler. Samples were prepared for X-ray diffraction (XRD) measurements by grinding the pellets in an agate mortar. A Panalytical Empyrean diffractometer in the Bragg-Brentano geometry was used. Phase analysis and lattice parameters were evaluated via Rietveld refinements with the General Structure Analysis System II software (GSASII). A goodness of fit value < 1.80% was achieved for all refinements.

Elemental composition with Energy Dispersive Spectroscopy (EDS)

EDS measurements were performed at the JIAM Electron Microscopy Facility with the collaboration of Dr. Dunlap. A Zeiss EVO MA15 Scanning Electron Microscope (SEM) equipped with a Bruker xFlash 6130 Energy Dispersive X-Ray Spectrometer (EDS) was used to analyze the microstructure and elemental composition of the samples.

Elemental composition with Electron Probe Microanalysis (EPMA)

EPMA measurements were performed at Electron Microprobe Laboratory in the

UT Earth and Planetary Sciences Department with the collaboration of Dr. McCanta and Dr. Patchen. A Cameca SX-100 electron microprobe was used to analyze the elemental composition of the samples. The instrument is equipped with 4 wavelength-dispersive spectrometers (WDS), and high-speed backscattered electron (BSE) detectors. The instrumental voltage and current were 15 kV and 30 nA, respectively. The probe size point is 2 μm and the excitation volume is in the 2 μm to 3 μm range. The instrument setup is similar to the one of an SEM. An EPMA bombards a microvolume of a sample with an electron beam. Image is obtained by detecting the backscattered electrons and compositional information is acquired by detecting characteristic x-rays by wavelength-dispersive spectroscopy (WDS). In WDS Bragg diffraction in a crystal is used to count the x-rays with a specific wavelength, while in EDS all wavelengths are detected at the same time. The advantages of WDS over EDS include a higher sensitivity due to a better x-ray peak resolution and greater peak to background ratio.

Oxidation state with X-ray photoelectron spectroscopy (XPS)

XPS measurements were performed at the JIAM Advanced Photoelectron Spectrometer Facility with the collaboration of Dr. Manella and Dr. Vilmercarti. XPS is used to verify the effectiveness of sintering atmospheres in changing the oxidation state of Ce and Pr. A SPECS Phoibos 150 hemispherical electron spectrometer and a SPECS Focus dual anode X-ray source were used to collect the XPS spectra of pellet samples. An in-vacuum file was used prior to the measurement to scrape the surface and expose the interior of the pellet in order to characterize the bulk portion.

In this technique the sample is irradiated with x-rays and the kinetic energy of the electrons that leave the top ~10 nm of material is measured. Elements with different oxidation state have different structure of the energy spectra. The oxidation state of lanthanides is usually assessed using the 3d spectra that contains multiplets corresponding to the spin-orbit split $3d_{5/2}$ and $3d_{3/2}$.

The spectra are composed of main peaks and satellite peaks. Main peaks correspond to the events when the outgoing electrons leave the atoms in the ground state; satellite peaks correspond to events when the outgoing electrons interact with valence electrons. When the outgoing electrons excite valence electrons and loses energy, the satellite will be seen at lower energies (shake-up satellite). When the outgoing electrons eject valence electrons, peaks are seen at higher energies (shake-off satellite).

CHAPTER FOUR
RESULTS AND DISCUSSION

Effects of composition on crystal structure of samples sintered in air

Compositions containing up to 5 types of cations can form a single crystal structure when sintered in air even when cooled slowly (3.3 ºC/min). The results of XRD phase analysis and Rietveld refinement are presented in Table 4.1. In that table, the samples are separated into four distinct groups depending on the presence or absence of Ce and Pr. The compositions written in bold correspond to single-phase samples. There is no clear trend between single-phase formation and average cationic radii. A maximum difference in cationic radii is also included in Table 4.1; this value was calculated as the percent difference in atomic radii between the largest and the smallest cation in each composition. No trend is observed between the maximum difference in cationic radii and the formation of a single structure as proposed by Tseng [41].

Table 4.1 shows that compositions with both Ce and Pr can form a single fluorite structure for samples containing of 3 or 4 cations. From the compositions containing 5 cations, two samples have a single C-type phase, namely (Ce,Gd,La,Pr,Y)O and (Ce,La,Pr,Sm,Y)O. All other samples with 5, 6, or 7 cations have a mixture of the C-type structure with either the A- or B-type phase. The fraction of the primary phase and the number of cations do not have a clear correlation.

From the group of samples containing Pr but not Ce, only (La,Pr)O and (La,Pr,Y)O have a single fluorite phase. In those two compositions there probably is an oxidation of Pr^{3+} to Pr^{4+} as the temperature increases [45] and PrO_2 acts as the parent structure into which the other oxides dissolve. In this same group of

samples, the compositions with 4, 5, and 6 cations have a mixture of the C- and B-type structures possibly because of the lower RE^{4+}/RE^{3+} ratio in those compositions.

From the group of samples containing Ce but not Pr, samples with 3 or 4 cations form a single C-type structure. This result indicates that for the samples with both Ce and Pr, Pr increases the RE^{4+}/RE^{3+} ratio and plays an important role in stabilizing the single fluorite structure. This argument is supported by the fact that samples without either Ce or Pr have a single monoclinic B-type phase for all the combinations of 3, 4 and 5 cations studied.

According to the results discussed this far, the addition of Ce in a composition does not determine whether the sample will form a single phase or not. This finding does not agree with Djenadic's work [36], which stated that a single fluorite phase was only formed when Ce was added in a composition. Their samples were prepared by the nebulized spray pyrolysis technique, not solid-state synthesis. Therefore, synthesis method influences phase formation.

The difference in synthesis temperature may explain why a given composition forms a single phase if synthesized by solid-state reaction, but not if synthesized by nebulized spray pyrolysis. Djenadic [36] synthesized nanoparticles at 1150°C while we use a sintering temperature of 1500ºC, therefore a higher temperature might be needed to induce the formation of a single structure. We test this point later in this thesis by investigating the phase evolution with sintering temperature of (Ce,La,Pr,Sm,Y)O.

In Djenadic's [36] work all Ce-containing compositions crystalized in a single phase, while some of our ceramics with 5 or more cations including Ce formed more than one phase. This could be explained by the fact that Djenadic's nanoparticles were collected on a relatively cold filter [44], [46], which would make this cooling process similar to air quenching. We test this point later in this thesis by studying the effects of fast cooling rate on two multiphase samples.

In Table 4.1 the unit cell volume varies consistently with the average ionic radii of the rare-earth elements. We systematically added new RE elements to the 3-element (Ce,La,Pr)O base compound to create a series of samples that each have 4 types of cations. Among these four samples, the unit cell volume increases according to the ionic radius of the RE cation added. By adding Y, we obtain (Ce,La,Pr,Y)O; this composition has a smaller unit cell volume than the 3 samples in which we added Gd, Sm, or Nd because the ionic radii increases in this respective order. Overall, the variation in unit cell volume in samples with different equiatomic combinations of cations is consistent with Vegard's law.

Reaction sequence between the raw binary oxides in (Ce,La,Pr,Sm,Y)O

In this section we investigate the reaction sequence between CeO_2, La_2O_3, Pr_2O_3, Sm_2O_3, and Y_2O_3 as they form the multicomponent oxide (Ce,La,Pr,Sm,Y)O. The goal is to determine at what temperature the binary oxides dissolve into the C-type phase and become stable in that structure at room temperature. Different pellets were sintered in a range of temperatures from 1000 to 1500ºC, always using a cooling rate of 3.3 ºC/min.

Figure 4.1.(a) and (b) show the XRD patterns of the pre-sintering mixture and the sintered samples showing increments of 100ºC and 50ºC in sintering temperature, respectively. The changes in crystal structure with increasing temperature can be summarized in the following list:

1) A comparison between the unreacted mixture and the sample sintered at 1000ºC (Figure 4.1.(a)) leads to a single remarkable difference: the reflections corresponding to Pr_2O_3 disappear due to the conversion of Pr_2O_3 (C-type) to PrO_2 (fluorite). When annealed in air, Pr_2O_3 is oxidized to Pr_6O_{11} (also a fluorite structure) at 275ºC [45] and then PrO_2 is formed at

temperatures greater than 500ºC [47].

2) From 1000 to 1200ºC, the reflection peaks of PrO_2 peaks become more intense than those of the other binary oxides. (Figure 4.1.(a))
3) At 1300ºC, all the reflection peaks start to merge towards the peaks of PrO_2. As the temperature increases, the positions of the most intense peaks of PrO_2 start matching with those that indicate the C-type structure in the sample sintered at 1500ºC, namely the (222), (004), (044), and (226) reflections.
4) At 1350ºC the peaks of CeO_2 and La_2O_3 disappear, indicating that they are the first oxides to be incorporated into the final structure (Figure 4.1.(b)). Peaks of Y_2O_3 are still seen at 1350ºC and Figure 4.1.(a) shows that there still are peaks of Sm_2O_3 at 1400ºC.
5) At 1400ºC only low intensity peaks of Y_2O_3 and Sm_2O_3 are observed, which indicates that those binary oxides are the last ones to be incorporated into the final C-type structure.
6) At 1450ºC (Figure 4.1.(b)) only the (222) reflection of the C-type structure is observed, indicating a complete reaction between the five initial binary oxides.

This same composition (Ce,La,Pr,Sm,Y)O was produced by Djenadic [36] in a reactor at 1150ºC, which indicates that the ideal synthesis temperature might differ between synthesis methods. It is important to notice that our ceramics were cooled to room temperature with a slow cooling rate (3.3 ºC/min), therefore 1450ºC is the temperature necessary to fully dissolve all the binary oxides into a single C-type structure and make it stable at room temperature using solid-state synthesis.

The sample sintered at 1500ºC was subjected to elemental composition analysis obtained by EDS spectra; the results are seen in Table 4.2. The ideal atomic concentration of the rare-earth elements is 8% for an equiatomic sesquioxide containing 5 cations. The rare-earth atomic concentration is in the 5.1% to 10.5% range in Table 4.2, indicating a close-to-equiatomic composition. The relative

amounts of oxygen and rare-earth elements also agree with the expected RE_2O_3 sesquioxide stoichiometry, indicating that the average oxidation state of the cations is close to 3+. The area examined and the homogeneous cation distribution in the EDS mapping are seen in Figure 4.2 (a) and Figure 4.2 (b), respectively.

A pellet of (Ce,La,Pr,Sm,Y)O sintered in air at 1500ºC for 10h was also examined using the electron microprobe analysis. Figure 4.3 shows the micrograph obtained and 8 areas evaluated for chemical composition. The 8 areas are indicated by red dots numbered from 1 to 8. Table 4.3 shows the chemical composition of those 8 areas. Areas 1, 2, 3, and 4 have a chemical composition that is close to the idealized for this sample, while areas 5, 6, 7, are rich in Sm and area 8 is rich in Y. This indicates that there are unreacted binary oxide particles in the sintered pellet that were not identified by XRD possibly due to their low concentration in the sample.

Effects of cooling rate on crystal structure

The assess the effects of cooling rate on phase stability, samples of the same composition were sintered in air and then either slowly cooled or quenched to room temperature in air. Two compositions were selected for this experiment: (Ce,Gd,La,Pr,Sm,Y)O and (Gd,La,Nd,Pr,Sm,Y)O. In Figure 4.4 their XRD patterns are compared to correlate the phases formed with the two different cooling approaches. (Ce,Gd,La,Pr,Sm,Y)O forms primary C-type and secondary B-type structures if cooled slowly; on the other hand, when quenched, this same composition has a single C-type phase, revealing that the C-type structure is the high-entropy stabilized phase at the sintering temperature of 1500ºC. (Gd,La,Nd,Pr,Sm,Y)O forms the C- and B- type structures if cooled slowly, but only the B-structure is formed when quenched, therefore only the B-type structure is present at high temperatures. Rapid cooling in these cases maintained the high-temperature single structure.

Effects of sintering atmosphere on crystal structure

Effects on oxidation state

In the compositional system being studied, only Ce and Pr can have two oxidation states: either 3+ or 4+; all the other rare-earths are 3+ (Table 1.1). In the raw oxides used, Ce and Pr have an oxidation of 4+ and 3+, respectively. The effectiveness of the sintering atmospheres in changing the oxidation state of Ce and Pr was assessed by comparing the XPS data of two samples of (Ce,La,Pr,Sm,Y)O, one sintered in air and the other in 2% H_2 in bulk N_2. Figure 4.5.(a) shows the Ce 3d region of the XPS spectra for both samples. The shape of both spectra is similar and they both have the s2' satellite peak that is characteristic of Ce^{4+} [48]. Therefore, there was not a complete reduction of all the Ce^{4+} to Ce^{3+}. Figure 4.5.(b) shows the Pr 3d region; in this case the higher intensity of the satellite peaks "s" and "s'" along with the presence of the structure "a'" in the sample sintered in air indicates the presence of Pr^{4+} [49], indicating that there was at least partial oxidation of the Pr cations during the synthesis process.

Figure 4.6 shows the change in color for four representative samples with different sintering atmospheres and composition. The color of (Ce,Gd,La,Nd,Pr,Sm,Y)O changes from dark brown (air) to dark orange (nitrogen) and then to lighter orange (2% hydrogen in bulk nitrogen). The change in oxidation state of the rare-earth ions may be associated with the changes in color seen in Figure 4.6. The darker samples are likely to have Pr^{4+}. (Ce,Gd,La,Nd,Sm,Y)O is light blue when sintered in air; the mixture of the binary oxides is also light blue. This same sample is mustard yellow when sintered in 2% H_2 in bulk N_2, which is similar to the color of Ce_2O_3, indicating that Ce is at least partially reduced from Ce^{4+} to Ce^{3+}. In (Gd,La,Nd,Pr,Sm,Y)O Ce is exchanged for Pr when compared to the previous sample. This change in composition leads to a green color in all sintering atmospheres, similar to the color of Pr_2O_3. The sample annealed in air is likely to have a higher Pr^{4+}/Pr^{3+} ratio and more intense color because the Pr^{4+} oxides are

darker than Pr^{3+} oxides. Removing both Ce and Pr leads to (Gd,La,Nd,Sm,Y)O in the bottom row of Figure 4.6. A stable blue color is observed as a result of the fact that all of the remaining elements have a stable 3+ oxidation state.

Effects on phase formation structure

In Figure 4.7 the XRD patterns of a series of representative compositions are compared across three sintering atmospheres. From the samples sintered in air, three of the four Ce- and Pr-containing samples form a single phase: (Ce,La,Pr)O, (Ce,La,Pr,Sm)O, and (Ce,La,Pr,Sm,Y)O. The first two compositions form a fluorite structure that is favored when Ce and Pr are in the 4+ state; in the last composition, adding Y^{3+} cations should decrease the RE^{4+}/RE^{3+} ratio, which favors the C-type structure.

When the three compositions discussed in the previous paragraph are sintered in an inert or reducing atmosphere (where Ce^{3+} and Pr^{3+} should be dominant) a primary C-type structure with a secondary A-type or B-type structure is formed. A higher relative intensity of the secondary phase peaks is observed for the reducing atmosphere.

In (Ce,Gd,La,Nd,Pr,Sm,Y)O, only Ce and Pr can have the 4+ oxidation state; consequently, this composition will have a lower RE^{4+}/RE^{3+} ratio, favoring a mixture of the B-type and C-type phases in all three sintering atmospheres instead of the fluorite phase. The monoclinic B-type structure seems to be favored by the reducing atmosphere since the relative intensity of the peaks corresponding to that phase is higher.

The phase analysis of (La,Pr,Y)O is the most surprising. In air this composition forms a single fluorite structure, which could be understood as the dissolution of La_2O_3 and Y_2O_3 into the fluorite structure of PrO_2. On the other hand, in either N_2 or 2%H_2 in bulk N_2, (La,Pr,Y)O forms a monoclinic B-type structure; however none

of the three rare-earth elements present in this composition form monoclinic oxides at atmospheric pressure [35], [50]. Therefore, the idea of one of the binary raw oxides acting as a parent crystal structure into which the other raw materials dissolve cannot be applied to the specific system of (La,Pr,Y)O and another explanation is required.

We refer to the phase diagram of polymorphic transformation for the lanthanoid sesquioxides (Figure 1.4) to propose an explanation on how (La,Pr,Y)O forms a monoclinic B-type structure. All the other samples that formed a single B-type structure in any of the sintering atmospheres have an average cationic radius in the range of 0.964 - 0.990 Å, Table 4.1. At 1500 ºC, this range lies mostly in the B-type region. The average ionic radius of the (La,Pr,Y)O is 0.989 Å, which lies in the A-type region close to the equilibrium line between the A- and B-type regions, possibly explaining formation of the B-type structure.

(Gd,La,Nd,Pr,Sm,Y)O forms a mixture of B- and C-type structures in air, and only the B-type is formed in nitrogen or 2% hydrogen in bulk nitrogen. This is consistent with the observations regarding the role of Pr charge state; in oxidizing atmosphere the cations of Pr^{4+} induce a cubic structure (C-type). In (Gd,La,Nd,Sm,Y)O, no oxidation state change can occur since the sample doesn't contain Ce or Pr, therefore the sintering atmosphere does not influence the phase formation.

From the results phase analysis in Figure 4.7 and Table 4.1, one can conclude that Ce and Pr form a cubic phase in an oxidizing atmosphere. In an inert or reducing atmosphere Ce, but not Pr, induces the formation of a cubic phase. In the absence of those two cations, various combinations of Gd, La, Nd, Sm, and Y form a single monoclinic structure for all atmospheres studied.

CHAPTER FIVE
CONCLUSION

The entropic contribution is not the only factor contributing to phase stabilization in multicomponent RE oxides. Solid-state sintering with surprisingly slow cooling rates can be used to synthesize single-phase ceramics, indicating that quenching is not necessary in this compositional space and no phase separation occurs during the cooling process.

The final crystal structure can be affected by the composition and the synthesis method. For the ceramics samples produced in this work, having Ce alone in the composition is not a determining factor for the formation of a single fluorite phase, as was the case in ceramics synthesized by the nebulized spray pyrolysis method [36]. However, the RE^{4+}/RE^{3+} ratio is higher in Ce-containing samples, favoring the formation of a cubic structure. In an oxidizing sintering atmosphere, both Ce and Pr contribute to the formation of a cubic phase in all the compositions studied; whereas in a reducing or inert atmosphere, only Ce favors a cubic structure. All samples without either Ce or Pr developed a single monoclinic structure.

Understanding how the composition, sintering atmosphere, and cooling rate influence the phase formation in multicomponent rare-earth oxide ceramics is important for the discovery of interesting functional properties in this system. As an example of possible future directions, an electronic band gap engineering approach might be applied to modify the position of the conduction and valence bands to accommodate a luminescence activator in order to produce efficient luminescent and scintillation function for applications in lighting, medical imaging, national security, and high energy physics.

CHAPTER SIX
FUTURE OUTLOOK

Future research will focus on testing the incorporation of binary oxides into a multicomponent single-phase sample by mixing raw materials with fully reacted single-phase multicomponent oxide powders followed by solid-state sintering.

The uniformity of cation distribution and the atomic positions of different species in single-phase samples should also be characterized with Transmission electron microscopy (TEM) Energy dispersive spectroscopy (EDS).

As an effort toward the exploration of the cocktail effect on functional properties, Ce and Pr should be used as luminescence activators in multicomponent compositions instead of having them as principal elements. Potential luminescence and scintillation properties will be investigated in those systems. Bandgap engineering and composition engineering will be applied in order to modify the position of the conduction band with respect to the excited states of the luminescence centers to produce efficient luminescence.

Multicomponent oxides will also be grown as single crystals by using a micro pulling down furnace for further investigation of crystal structure and functional properties.

LIST OF REFERENCES

[1] M. C. Gao, J.-W. Yeh, P. K. Liaw, and C. Zhang, *High-Entropy Alloys: Fundamentals and Applications*. Springer Switzerland, 2016.
[2] B. S. Murty, J. W. Yeh, and S. Ranganathan, *High-Entropy Alloys*. Butterworth-Heinemann Elsevier, 2014.
[3] B. Cantor, I. T. H. Chang, P. Knight, and A. J. B. Vincent, "Microstructural development in equiatomic multicomponent alloys," *Mater. Sci. Eng. A*, vol. 375–377, no. 1–2 SPEC. ISS., pp. 213–218, 2004.
[4] J.-W. Yeh *et al.*, "Nanostructured High-Entropy Alloys with Multiple Principal Elements: Novel Alloy Design Concepts and Outcomes," *Adv. Eng. Mater.*, vol. 6, no. 5, pp. 299–303, 2004.
[5] F. Otto, Y. Yang, H. Bei, and E. P. George, "Relative effects of enthalpy and entropy on the phase stability of equiatomic high-entropy alloys," *Acta Mater.*, vol. 61, no. 7, pp. 2628–2638, 2013.
[6] D. . Miracle and O. N. Senkov, "A critical review of high entropy alloys and related concepts," *Acta Mater.*, vol. 122, no. October, pp. 448–511, 2017.
[7] S. Varalakshmi, M. Kamaraj, and B. S. Murty, "Formation and stability of equiatomic and nonequiatomic nanocrystalline CuNiCoZnAlTi high-entropy alloys by mechanical alloying," *Metall. Mater. Trans. A Phys. Metall. Mater. Sci.*, vol. 41A, no. 10, pp. 2703–2709, 2010.
[8] W. Chen, Z. Fu, S. Fang, Y. Wang, H. Xiao, and D. Zhu, "Processing, microstructure and properties of Al0.6CoNiFeTi0.4 high entropy alloy with nanoscale twins," *Mater. Sci. Eng. A*, vol. 565, pp. 439–444, 2013.
[9] C. Wang, W. Ji, and Z. Fu, "Mechanical alloying and spark plasma sintering of CoCrFeNiMnAl high-entropy alloy," *Adv. Powder Technol.*, vol. 25, pp. 1334–1338, 2014.
[10] B. Gludovatz, A. Hohenwarter, D. Catoor, E. H. Chang, E. P. George, and R. O. Ritchie, "A Fracture-Resistant High-Entropy Alloy for Cryogenic Applications.," *Science (80-.).*, vol. 345, no. 6201, pp. 1153–1158, 2014.
[11] A. Gali and E. P. George, "Tensile properties of high- and medium-entropy alloys," *Intermetallics*, vol. 39, pp. 74–78, 2013.
[12] C. W. Tsai, M. H. Tsai, J. W. Yeh, and C. C. Yang, "Effect of temperature on mechanical properties of Al0.5CoCrCuFeNi wrought alloy," *J. Alloys Compd.*, vol. 490, pp. 160–165, 2010.
[13] K. Jin and H. Bei, "Single-Phase Concentrated Solid-Solution Alloys: Bridging Intrinsic Transport Properties and Irradiation Resistance," *Front. Mater.*, vol. 5, no. April, pp. 1–11, 2018.
[14] Y.-F. Kao, S.-K. Chen, T.-J. Chen, P.-C. Chu, J.-W. Yeh, and S.-J. Lin, "Electrical, magnetic, and Hall properties of AlxCoCrFeNi high-entropy alloys," *J. Alloys Compd.*, vol. 509, no. 5, pp. 1607–1614, 2011.
[15] H. P. Chou, Y. S. Chang, S. K. Chen, and J. W. Yeh, "Microstructure, thermophysical and electrical properties in AlxCoCrFeNi ($0 \leq x \leq 2$) high-entropy alloys," *Mater. Sci. Eng. B Solid-State Mater. Adv. Technol.*, vol. 163, no. 3, pp. 184–189, 2009.
[16] S. Maiti *et al.*, "Discovery of a Superconducting High-Entropy Alloy," *Phys.*

Rev. Lett., vol. 113, no. 10, pp. 1–5, 2014.
[17] S. Vrtnik *et al.*, “Superconductivity in thermally annealed Ta-Nb-Hf-Zr-Ti high-entropy alloys,” *J. Alloys Compd.*, vol. 695, pp. 3530–3540, 2017.
[18] Y. Zhang, T. Zuo, Y. Cheng, and P. K. Liaw, “High-entropy alloys with high saturation magnetization, electrical resistivity, and malleability,” *Sci. Rep.*, vol. 3, pp. 1–7, 2013.
[19] A. J. Zaddach *et al.*, “Structure and magnetic properties of a multi-principal element Ni–Fe–Cr–Co–Zn–Mn alloy,” *Intermetallics*, vol. 68, pp. 107–112, 2016.
[20] J. W. Yeh, “Alloy design strategies and future trends in high-entropy alloys,” *JOM*, vol. 65, no. 12, pp. 1759–1771, 2013.
[21] C. H. Lai, K. H. Cheng, S. J. Lin, and J. W. Yeh, “Mechanical and tribological properties of multi-element (AlCrTaTiZr)N coatings,” *Surf. Coatings Technol.*, vol. 202, no. 15, pp. 3732–3738, 2008.
[22] M. Braic, V. Braic, M. Balaceanu, C. N. Zoita, A. Vladescu, and E. Grigore, “Characteristics of (TiAlCrNbY)C films deposited by reactive magnetron sputtering,” *Surf. Coatings Technol.*, vol. 204, pp. 2010–2014, 2010.
[23] J. Gild *et al.*, “High-Entropy Metal Diborides: A New Class of High-Entropy Materials and a New Type of Ultrahigh Temperature Ceramics,” *Sci. Rep.*, vol. 6, no. 1, pp. 1–10, 2016.
[24] C. M. Rost *et al.*, “Entropy-stabilized oxides,” *Nat. Commun.*, vol. 6, no. 8485, 2015.
[25] M. C. Gao, D. B. Miracle, D. Maurice, X. Yan, Y. Zhang, and J. A. Hawk, “High-entropy functional materials,” *J. Mater. Res.*, vol. 33, no. 19, pp. 3138–3155, 2018.
[26] D. Bérardan, S. Franger, D. Dragoe, A. K. Meena, and N. Dragoe, “Colossal dielectric constant in high entropy oxides,” *Phys. Status Solidi - Rapid Res. Lett.*, vol. 10, no. 4, pp. 328–333, 2016.
[27] D. Bérardan, S. Franger, A. K. Meena, and N. Dragoe, “Room temperature lithium superionic conductivity in high entropy oxides,” *J. Mater. Chem. A*, vol. 4, pp. 9536–9541, 2016.
[28] P. B. Meisenheimer, T. J. Kratofil, and J. T. Heron, “Giant enhancement of exchange coupling in entropy-stabilized oxide heterostructures,” *Sci. Rep.*, vol. 7, no. 1, pp. 1–6, 2017.
[29] R. Witte *et al.*, “High entropy oxides: An emerging prospect for magnetic rare earth - transition metal perovskites,” *Phys. Rev. Mater.*, vol. 3, no. 034406, pp. 1–8, 2019.
[30] Y. Sharma *et al.*, “Single-crystal high entropy perovskite oxide epitaxial films,” *Phys. Rev. Mater.*, vol. 2, no. 6, p. 060404, 2018.
[31] J. L. Braun *et al.*, “Charge-Induced Disorder Controls the Thermal Conductivity of Entropy-Stabilized Oxides,” *Adv. Mater.*, vol. 30, pp. 1–8, 2018.
[32] J. Gild *et al.*, “High-entropy fluorite oxides,” *J. Eur. Ceram. Soc.*, vol. 38, no. 10, pp. 3578–3584, 2018.

[33] A. Sarkar *et al.*, “High entropy oxides for reversible energy storage,” *Nat. Commun.*, vol. 9, pp. 1–9, 2018.
[34] H. Chen *et al.*, “Entropy-stabilized metal oxide solid solutions as CO oxidation catalysts with high-temperature stability,” *J. Mater. Chem. A*, vol. 6, no. 24, pp. 11129–11133, 2018.
[35] G. Adachi and Z. C. Kang, *Lanthanides, Tantalum and Niobium*. New York, Berlin: Springer-Verlag Berlin Heidelberg GmbH, 1989.
[36] R. Djenadic *et al.*, “Multicomponent equiatomic rare earth oxides,” *Mater. Res. Lett.*, vol. 5, no. 2, pp. 102–109, 2017.
[37] S. Jiang *et al.*, “A new class of high-entropy perovskite oxides,” *Scr. Mater.*, vol. 142, pp. 116–120, 2018.
[38] J. Dąbrowa *et al.*, “Synthesis and microstructure of the (Co,Cr,Fe,Mn,Ni)3O4 high entropy oxide characterized by spinel structure,” *Mater. Lett.*, vol. 216, pp. 32–36, 2018.
[39] K. Chen *et al.*, “A five-component entropy-stabilized fluorite oxide,” *J. Eur. Ceram. Soc.*, vol. 38, no. 11, pp. 4161–4164, 2018.
[40] A. Sarkar *et al.*, “Multicomponent equiatomic rare earth oxides with a narrow band gap and associated praseodymium multivalency,” *Dalt. Trans.*, vol. 46, no. 36, pp. 12167–12176, 2017.
[41] K. Tseng, Q. Yang, S. J. McCormack, and W. M. Kriven, “High-entropy, phase-constrained, lanthanide sesquioxide,” *J. Am. Ceram. Soc.*, no. December 2018, pp. 1–8, 2019.
[42] G. Y. Adachi and N. Imanaka, “The binary rare earth oxides,” *Chem. Rev.*, vol. 98, no. 4, pp. 1479–1514, 1998.
[43] R. D. Shannon and C. T. Prewitt, “Effective ionic radii in oxides and fluorides,” *Acta Crystallogr. Sect. B Struct. Crystallogr. Cryst. Chem.*, vol. 25, no. 5, pp. 925–946, 1969.
[44] R. Djenadic *et al.*, “Nebulized spray pyrolysis of Al-doped Li7La3Zr 2O12 solid electrolyte for battery applications,” *Solid State Ionics*, vol. 263, pp. 49–56, 2014.
[45] S. C. Atkinson, “Crystal Structures and Phase Transitions in the Rare Earth Oxides,” University of Salford, 2013.
[46] R. Djenadic, M. Botros, and H. Hahn, “Is Li-doped MgAl2O4 a potential solid electrolyte for an all-spinel Li-ion battery?,” *Solid State Ionics*, vol. 287, pp. 71–76, 2016.
[47] B. G. Hyde, E. E. Garver, U. E. Kuntz, and L. Eyring, “Kinetic studies on reactions of praseodymium oxides in an oxygen atmosphere: PrO1.83 + O2 ⇄ PrO2,” *J. Phys. Chem.*, vol. 69, no. 5, pp. 1667–1675, 1965.
[48] E. Bêche, P. Charvin, D. Perarnau, S. Abanades, and G. Flamant, “Ce 3d XPS investigation of cerium oxides and mixed cerium oxide (Ce xTiyOz),” *Surf. Interface Anal.*, vol. 40, no. 3–4, pp. 264–267, 2008.
[49] M. Y. Sinev, G. W. Graham, L. P. Haack, and M. Shelef, “Kinetic and structural studies of oxygen availability of the mixed oxides Pr1-xMxOy (M = Ce,Zr),” *J. Mater. Res.*, vol. 11, no. 8, pp. 1960–1971, 1996.

[50] H. R. Hoekstra and K. A. Gingerich, “High-Pressure B-Type Polymorphs of Some Rare-Earth Sesquioxides,” *Science (80-.).*, vol. 146, no. 3648, pp. 1163–1164, 1964.

APPENDIX

Tables

Table 1.1. Ionic radii correlated to coordination number, crystal structure, and oxidation state of rare-earth cations in dioxides and sesquioxides [42], [43].

Binary Oxide	Cation oxidation state	Crystal structure	Coordination number	Ionic radius (Å)
CeO_2	4+	Fluorite	VIII	0.80
Ce_2O_3	3+	A-type	VII	1.09*
		C-type	VI	1.034
Gd_2O_3	3+	B-type	VI and VII	0.938 and 0.999*
		C-type	VI	0.938
La_2O_3	3+	A-type	VII	1.10
		C-type	VI	1.061
Nd_2O_3	3+	A-type	VII	1.06*
		C-type	VI	0.995
PrO_2	4+	Fluorite	VIII	0.78
Pr_2O_3	3+	A-type	VII	1.08*
		C-type	VI	1.013
Sm_2O_3	3+	A-type	VII	1.03*
		B-type	VI and VII	0.964 and 1.03*
		C-type	VI	0.964
Y_2O_3	3+	C-type	VI	0.892

* Values interpolated from ionic radii for coordination VI and VIII

Table 3.1. Details of raw materials used for sample preparation

Raw material	Initial crystal structure	Manufacturer	Purity (%)
CeO_2	Fluorite	American Elements	99.999
Gd_2O_3	C-type	American Elements	99.999
La_2O_3	A-type	Sigma Aldrich	99.999
Nd_2O_3	A-type	Sigma Aldrich	99.99
Pr_2O_3	C-type	Sigma Aldrich	99.9
Sm_2O_3	B-type	Alfa Aesar	99.99
Y_2O_3	C-type	Yarmouth Materials	99.9

Table 3.2. Examples of compositions produced in this work. Four distinct groups can be seen based on the presence or absence of Ce and Pr

Sample	Number of cations
(Ce,La,Pr)O	3
(Ce,La,Pr,Sm,Y)O	5
(Ce,Gd,La,Nd,Pr,Sm,Y)O	7
(La,Pr)O	2
(La,Nd,Pr,Y)O	4
(Gd,La,Nd,Pr,Sm,Y)O	6
(Ce,Gd,La)O	3
(Ce,Gd,La,Sm,Y)O	5
(Ce,Gd,La,Nd,Sm,Y)O	6
(Gd,La,Sm)O	3
(La,Nd,Sm,Y)O	4
(Gd,La,Nd,Sm,Y)O	5

Table 4.1. Phase analysis and Rietveld refinement results for the samples sintered in air and cooled at 3.3ºC/min. Single phase samples are written in bold; regular font indicates the presence of multiple phases. Cation radii used for calculations corresponded to coordination number VII. The % difference in cation radii is calculated using the largest and the smallest rare-earth cationic radii as $\frac{\text{largest}-\text{smallest}}{\text{largest}}.100\%$

Sample	**% difference in cation radii**	**Average cation radius *(Å)***	**Crystalline phases**	**Unit cell volume ($Å^3$)**	**Fraction of primary phase (%)**
Compositions with Ce and Pr					
(Ce,La,Pr)O	**4.5**	**1.036**	**Fluorite**	**166.94(4)**	**100**
(Ce,Gd,La,Pr)O	**11.6**	**1.012**	**Fluorite**	**166.51(6)**	**100**
(Ce,La,Nd,Pr)O	**6.2**	**1.026**	**Fluorite**	**168.46(0)**	**100**
(Ce,La,Pr,Sm)O	**9.1**	**1.018**	**Fluorite**	**167.24(0)**	**100**
(Ce,La,Pr,Y)O	**15.9**	**1.000**	**Fluorite**	**164.77(7)**	**100**
(Ce,Gd,La,Nd,Pr)O	11.6	1.008	C-type	1333.62(3)	91
			A-type	89.28(8)	
(Ce,Gd,La,Pr,Sm)O	11.6	1.002	C-type	1323.15(7)	80
			B-type	478.19(1)	
(Ce,Gd,La,Pr,Y)O	**15.9**	**0.988**	**C-type**	**1302.09(9)**	**100**
(Ce,La,Nd,Pr,Sm)O	9.1	1.013	C-type	1338.24(8)	94
			A-type	89.46(0)	
(Ce,La,Nd,Pr,Y)O	15.9	0.999	C-type	1320.75(7)	86
			B-type	441.80(9)	
(Ce,La,Pr,Sm,Y)O	**15.9**	**0.992**	**C-type**	**1310.49(9)**	**100**
(Ce,Gd,La,Nd,Pr,Sm)O	11.6	1.001	C-type	1326.58(0)	70
			B-type	472.67(2)	
(Ce,Gd,La,Nd,Pr,Y)O	15.9	0.988	C-type	1309.25(2)	71
			B-type	465.36(3)	
(Ce,Gd,La,Pr,Sm,Y)O	15.9	0.984	C-type	1300.40(8)	89
			B-type	451.22(6)	
(Ce,La,Nd,Pr,Sm,Y)O	15.9	0.993	C-type	1314.49(4)	76
			B-type	455.17(0)	
(Ce,Gd,La,Nd,Pr,Sm,Y)O	15.9	0.985	C-type	1308.12(9)	82
			B-type	465.61(1)	
Samples without Ce and with Pr					
(La,Pr)O	**4.5**	**1.037**	**Fluorite**	**172.21(4)**	**100**
(La,Pr,Y)O	**15.9**	**0.989**	**Fluorite**	**165.87(8)**	**100**
(Gd,La,Pr,Y)	15.9	0.976	C-type	1304.05(7)	57
			B-type	463.22(6)	

Table 4.1. Continued.

Sample	**% difference in cation radii**	**Average cation radius *(Å)***	**Crystalline phases**	**Unit cell volume ($Å^3$)**	**Fraction of primary phase (%)**
(La,Nd,Pr,Y)O	15.9	0.990	C-type	1329.79(2)	69
			B-type	472.39(9)	
(La,Pr,Sm,Y)O	15.9	0.983	C-type	1311.76(7)	71
			B-type	464.79(4)	
(Gd,La,Nd,Pr,Sm)O	11.6	0.994	C-type	1307.34(7)	
			B-type	464.24(6)	51
(Gd,La,Nd,Pr,Sm,Y)O	15.9	0.977	C-type	1331.08(0)	
			B-type	475.70(3)	65
Samples with Ce and without Pr					
(Ce,Gd,La)O	**11.6**	**1.011**	**C-type**	**1345.66(1)**	**100**
(Ce,La,Sm,Y)O	**15.9**	**0.988**	**C-type**	**1317.43(7)**	**100**
(Ce,Gd,La,Sm,Y)O	15.9	0.978	C-type	1312.82(1)	61
			B-type	456.19(3)	
(Ce,Gd,La,Nd,Sm,Y)O	15.9	0.981	C-type	1325.61(7)	91
			B-type	459.03(1)	
Samples without Ce and Pr					
(Gd,La,Sm)O	**11.6**	**0.988**	**B-type**	**461.75(5)**	**100**
(La,Nd,Y)O	**15.9**	**0.983**	**B-type**	**464.32(2)**	**100**
(Gd,La,Nd,Sm)O	**11.6**	**0.990**	**B-type**	**462.88(2)**	**100**
(La,Nd,Sm,Y)O	**15.9**	**0.978**	**B-type**	**457.58(9)**	**100**
(Gd,La,Sm,Y)O	**15.9**	**0.964**	**B-type**	**449.50(5)**	**100**
(Gd,La,Nd,Sm,Y)O	**15.9**	**0.970**	**B-type**	**464.58(8)**	**100**

Table 4.2. Elemental composition of (Ce,La,Pr,Sm,Y)O obtained from EDS spectra.

Element	Composition (at%)
Ce	10.5 ± 0.6
La	8.2 ± 0.4
Pr	9.2 ± 0.5
Sm	5.1 ± 0.3
Y	60 ± 1

Table 4.3. Elemental composition of (Ce,La,Pr,Sm,Y)O obtained from EPMA. The eight areas probed are shown in Figure 4.3. Areas 1-4 have a chemical composition close to ideal. Areas 5-8 have a higher concentration of one of the cations (data in red), indicating the presence of unreacted raw material.

Area probed	Elemental composition (at%)					
	Ce	La	Pr	Sm	Y	O
1	8.4	12.7	3.9	5.0	8.4	61.6
2	11.2	8.3	8.2	4.5	5.5	62.3
3	10.7	7.9	7.4	3.5	8.3	62.2
4	7.3	10.1	6.2	4.1	10.8	61.5
5	0.3	1.9	1.6	34.6	1.5	60.1
6	0.2	1.0	0.7	37	0.4	60.7
7	0.0	0.0	0.0	40.0	0.0	60.0
8	1.6	1.6	1.6	0.9	34.7	59.6

Figures

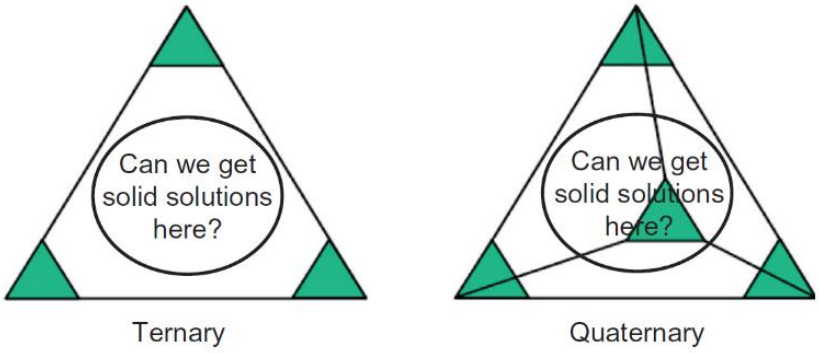

Figure 1.1. Schematic ternary and quaternary phase diagrams of traditional alloys. The green regions near the corners are relatively well known, while the central region is not explored [2].

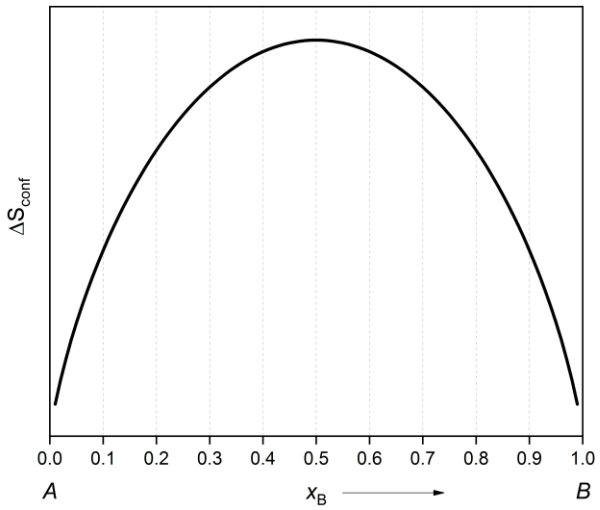

Figure 1.2. Configurational entropy as a function of molar composition of a system containing two components: A and B

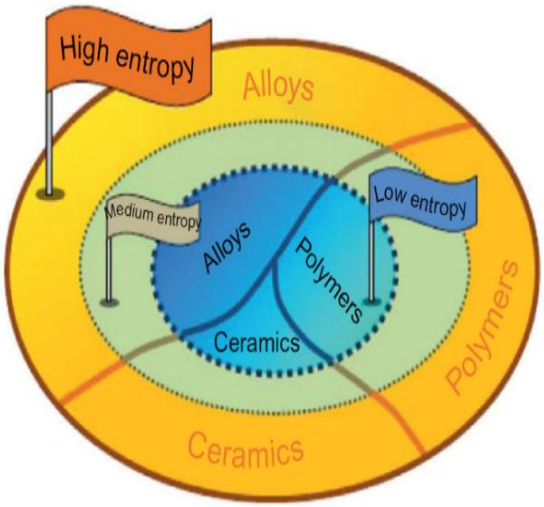

Figure 1.3. Materials world based on configurational entropy. The mixing entropy effect of HEA is expected in ceramics and polymers [2].

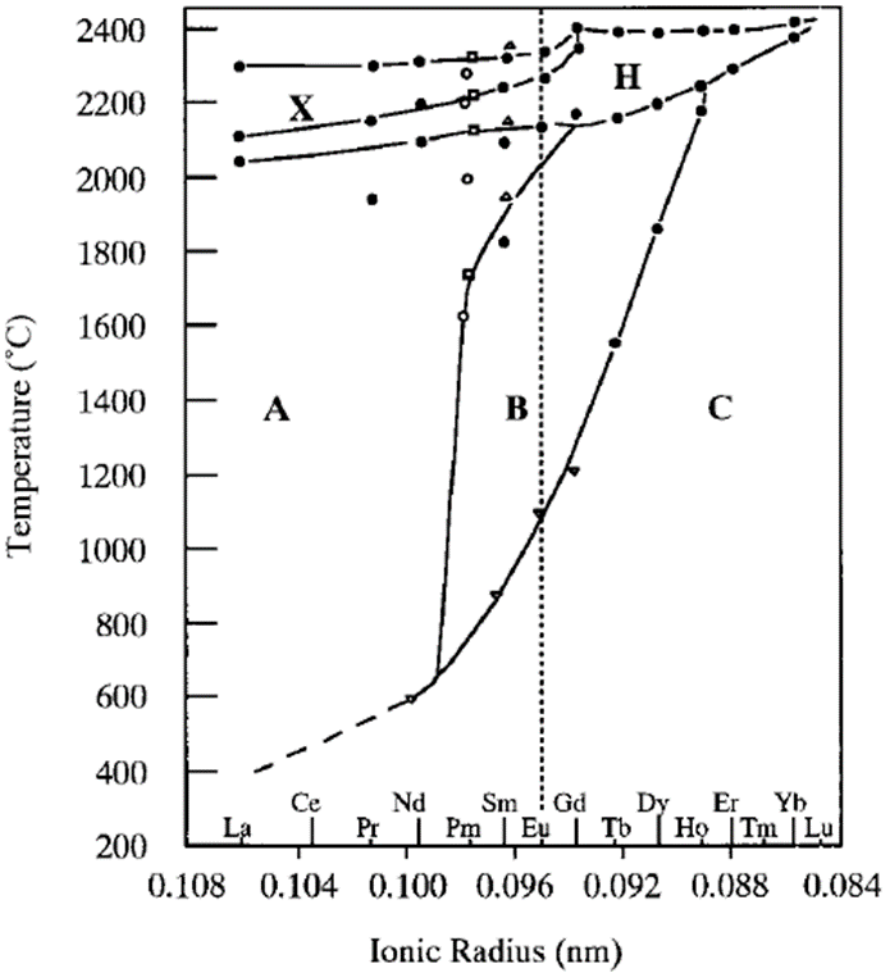

Figure 1.4. Polymorphic transformation of the lanthanide sesquioxides [36].

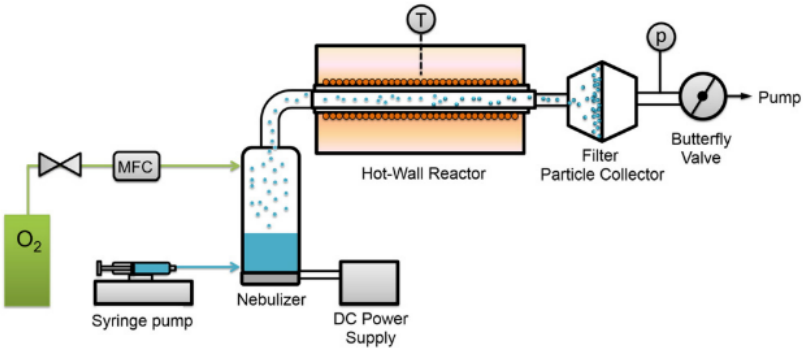

Figure 1.5. Schematic representation of the nebulized spray pyrolysis setup [44].

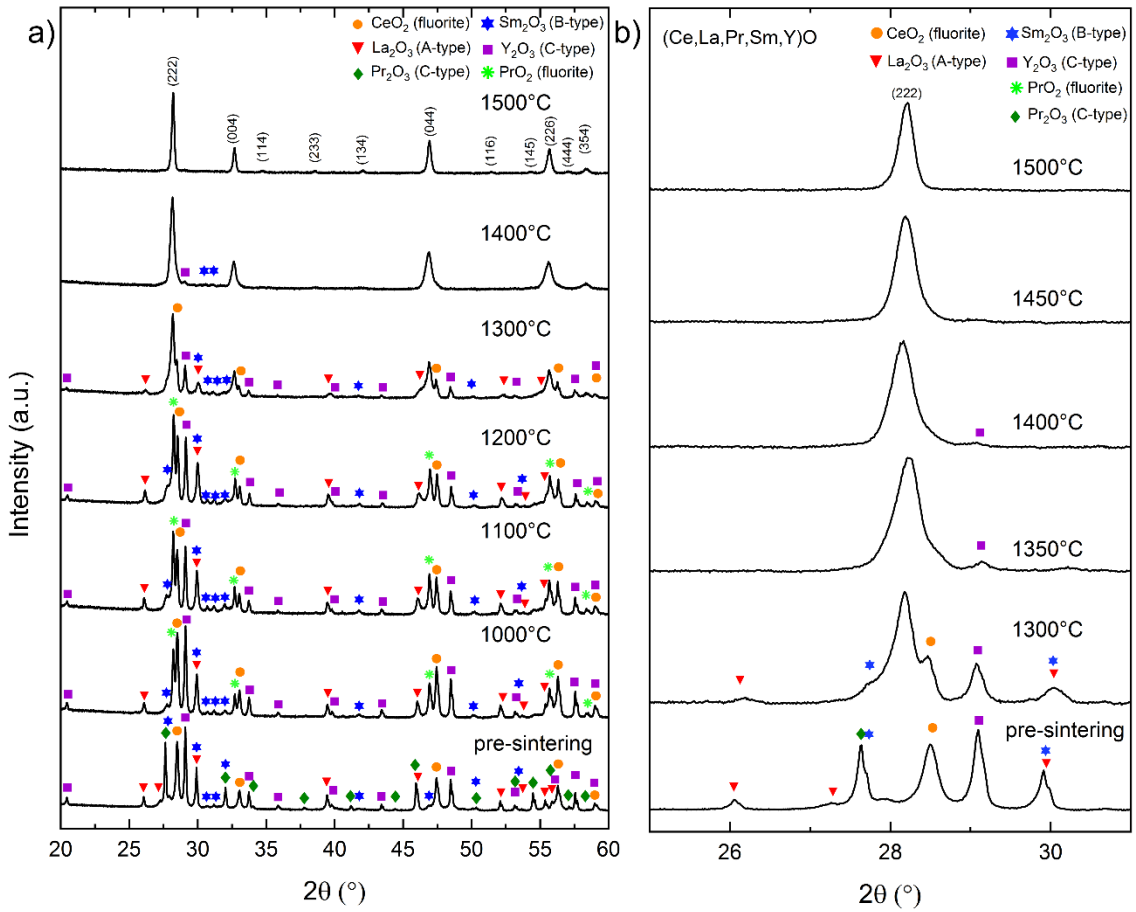

Figure 4.1. (a) Powder XRD patterns of (Ce,La,Pr,Sm,Y)O samples sintered in air at temperatures from 1000ºC to 1500ºC. XRD patterns were obtained at room temperature. (b) Expansion of the 2θ scale showing the formation of the (222) reflection peak. Peaks corresponding to the binary oxide phases are labeled by symbols as shown in the legend.

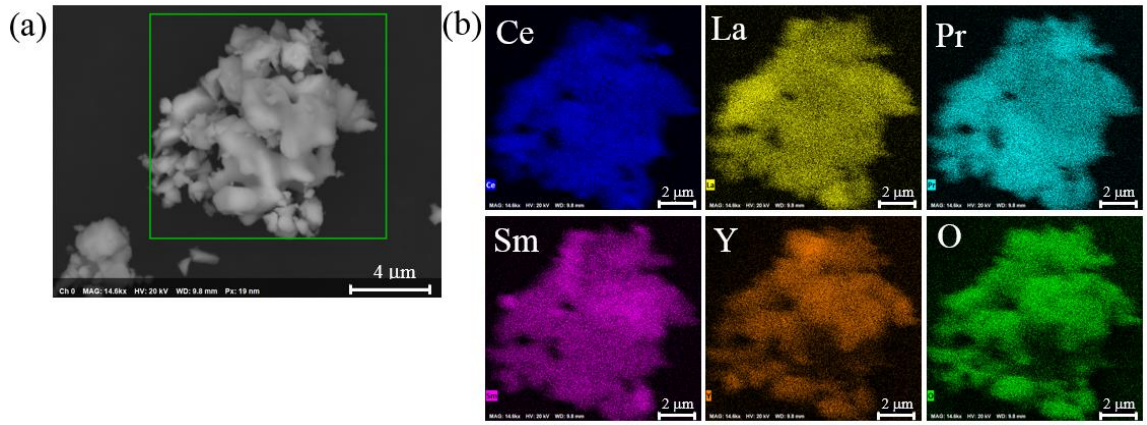

Figure 4.2. (a) SEM image of (Ce,La,Pr,Sm,Y)O sintered in air at 1500 ºC showing a very dense microstructure. (b) Individual EDS maps show a homogeneous distribution of the 5 cations. The color coding is used for clarity of the representation.

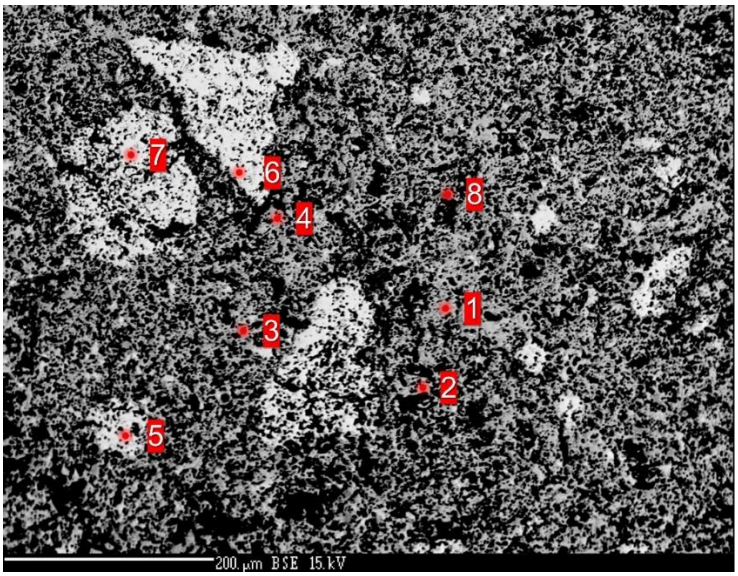

Figure 4.3. Electron microprobe micrograph of a (Ce,La,Pr,Sm,Y)O pellet. The areas surveyed for chemical composition are numbered from 1 to 8.

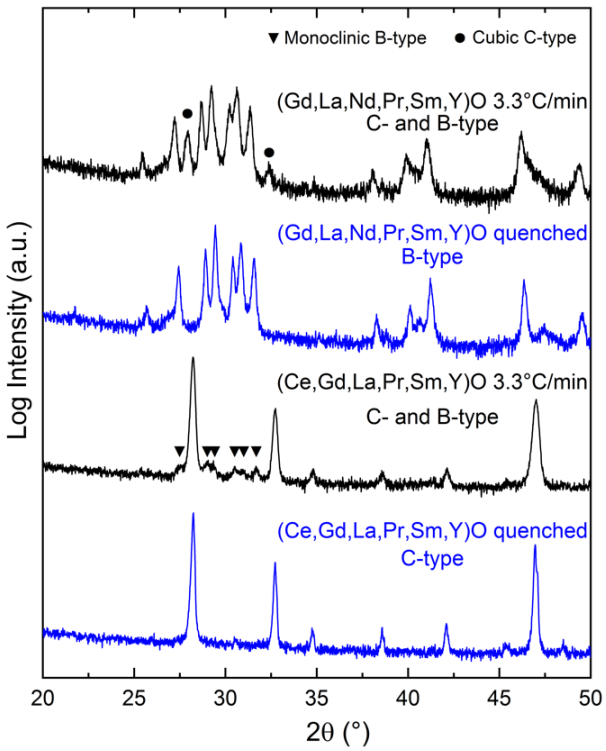

Figure 4.4. Powder XRD patterns of samples sintered in air and submitted to either a slow cooling of 3.3ºC/min or quenching in air. Peaks corresponding to secondary phases are labeled by symbols as shown in the legend.

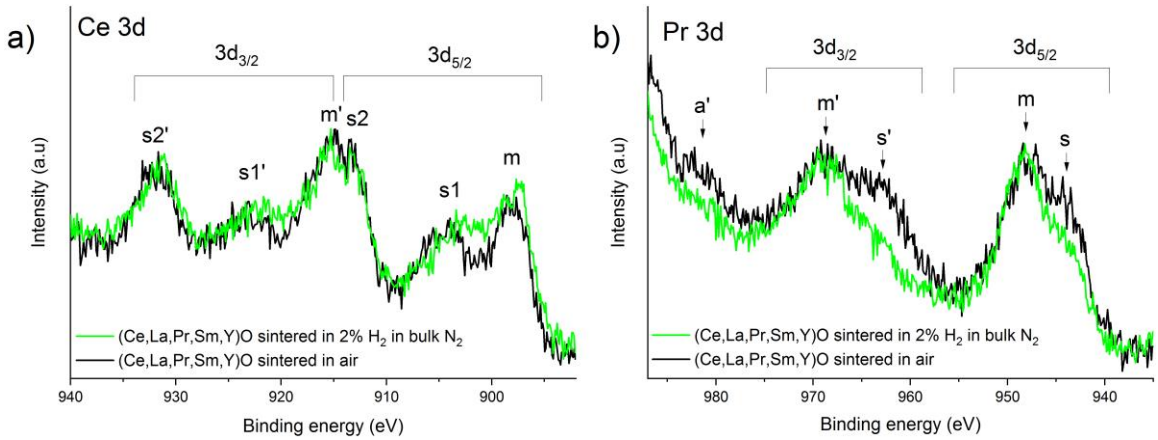

Figure 4.5. (a) Ce 3d region and (b) Pr 3d region of XPS spectra of 2 (Ce,La,Pr,Sm,Y)O samples. Black and green spectra correspond to sample sintered in an oxidizing and a reducing atmosphere, respectively. Peak identifications starting with “m” refer to main peaks while those starting with “s” refer to satellite peaks. The s2’ peak in the Ce 3d region (a) indicates the presence of Ce^{4+} in both samples. In the Pr 3d region (b), the higher intensity of the satellite peaks and the presence of the structure a’ indicates the presence of Pr^{4+}.

Figure 4.6. Photographs of ground sintered samples comparing the change in color with composition and sintering atmosphere.

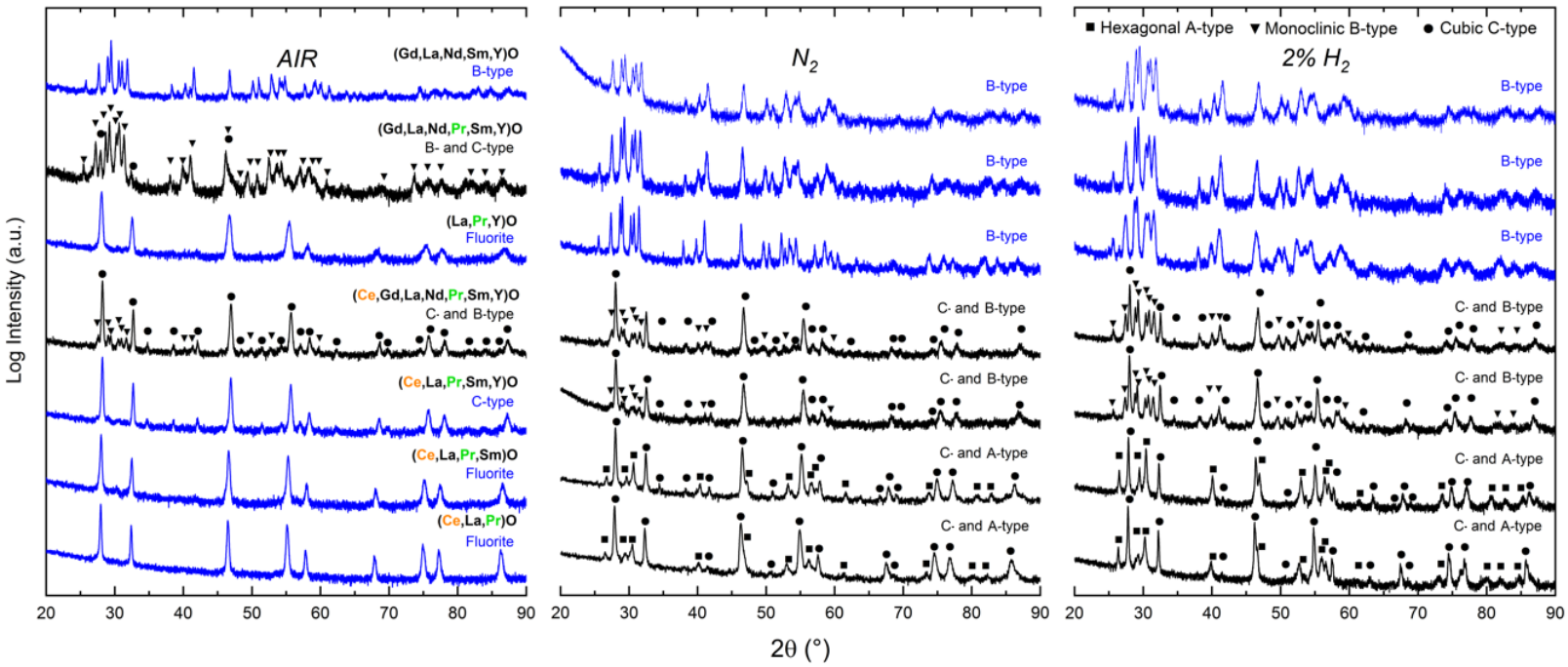

Figure 4.7. XRD patterns of selected compositions comparing the effects of sintering atmosphere on phase formation. The compositions and their vertical order are the same for each group of XRD patterns. Blue patterns correspond to single-phase samples

VITA

Matheus Pianassola was born in São José dos Campos, Brazil, where he spent his first 21 years. In 2008 he received a full scholarship to study at Embraer High School, one of the best-ranked schools in Brazil. In that high school, he received the necessary support to pass the entrance exams of four of the most competitive public universities in Brazil. He pursued his bachelor's degree in Science and Technology at the Federal University of São Paulo, becoming a proud first-generation college student. In 2014 he received a full scholarship from the Brazilian Science Without Borders mobility program and spent a year at the University of Tennessee where he took engineering classes and worked as an undergraduate researcher. Matheus received his second bachelor's degree in Materials Engineering in 2017 and is currently pursuing his PhD degree also in Materials Engineering at The University of Tennessee, Knoxville.